Origin of Unexpected Products from CO2 Electroreduction on Silver: The Role of ppb-Level Copper Impurities in the Electrolyte

ACS Electrochemistry

pubs.acs.org/electrochem

Article

Origin of Unexpected Products from CO_2 Electroreduction on Silver: The Role of ppb-Level Copper Impurities in the Electrolyte

Chaoqun Ma, Flora Haun, Federico Dattila, Wankai Tang, Gumaa A. El-Nagar, Ajin Anilkumar, Simelys Hernández, and Matthew T. Mayer*

Cite This: https://doi.org/10.1021/acselectrochem.6c00077

Read Online

ACCESS | Metrics & More | Article Recommendations | Supporting Information

ABSTRACT: Silver (Ag) electrodes are among the best catalysts for producing CO in electrochemical CO_2 reduction (CO_2R). Beyond the catalyst material, it is increasingly recognized that electrolyte effects and dynamic processes that shape the interfacial microenvironment play critical roles in determining product selectivity. Herein, we reported unique observations of a variety of other CO_2R products from Ag foil electrodes, highly dependent on electrolyte concentration and impurities. Notably, we found that trace levels of Cu (<5 ppb) could induce significant selectivity toward methane (CH_4). This suggested that (sub)monolayer amounts of impurity metal deposited on Ag electrodes can drastically alter product selectivity. Density functional theory attributed this surprising CH_4 selectivity to a d-band center upshift induced by the lattice mismatch with the Ag substrate. We furthermore observed that product selectivity shifts significantly over time during extended testing, attributable to dynamic electrolyte changes enabled by cation-exchange membranes. This study offers new insights into the behavior of well-studied Ag catalysts, highlighting the importance of trace electrolyte constituents and suggesting a possible new strategy for selectivity tuning.

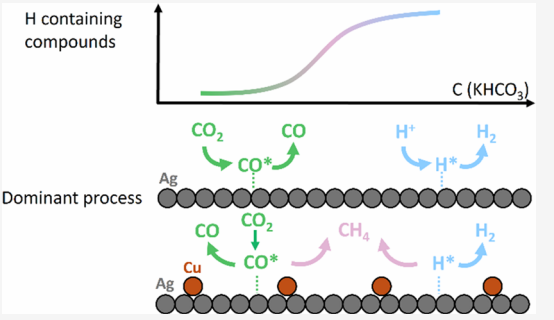

KEYWORDS: *electrochemical CO_2 reduction, Ag electrode, electrolyte impurities, ppb-level impurities, unexpected products, cation crossover*

INTRODUCTION

Among catalysts for electrochemical CO_2 reduction (CO_2R) to value-added products, silver is one of the most effective for the selective production of carbon monoxide as the main product.[1] Selectivities (in terms of Faradaic efficiency, FE) reaching nearly 100% have repeatedly been achieved, and recent progress in developing scalable Ag-based electrolyzers shows that there is great promise for this technology for sustainable carbon monoxide (CO) production,[2] a key industrial chemical used, for instance, in Fischer−Tropsch synthesis of hydrocarbons. Many detailed studies have advanced our understanding of electrode materials for CO_2R, focusing on product selectivity,[3−7] mass transfer effects,[8,9] and catalyst modification,[3,10] such as material synthesis and morphology tuning, to improve the performance.[11−14] Furthermore, gas diffusion electrode-based electrolyzers using Ag catalysts have been demonstrated to produce CO selectively at high rates, at increasingly large scales and promising durability, representing one of the highest technology readiness levels among low-temperature CO_2R pathways.[15−17]

Despite the widespread use of Ag electrodes for highly selective CO production, only a few studies have reported the formation of products other than CO, purportedly induced by specific operating conditions or material modifications. Dutta et al. reported that an Ag foam electrode prepared by electrochemical deposition exhibited high selectivity toward hydrocarbons.[12] This shift in selectivity was attributed to the electrode's high surface area and porosity, which were proposed to enhance the surface concentration of the CO* intermediate. Raaijman et al. found that pressurized CO feeds could induce the formation of C_{2-3} alcohols on Ag.[18] Shiratsuchi and Nogami demonstrated that a pulsed potential electrolysis using a polycrystalline Ag foil electrode can generate hydrocarbons (CH_4 and ethylene C_2H_4) at high FE, which they attributed to altered coverage of adsorbed intermediate species relative to potentiostatic operation.[19]

The aforementioned studies reveal that the surface structure, local environment, adsorbates, and mass-transport phenomena all seem important in triggering pathways to products beyond CO on Ag. We noted, however, that electrolyte effects for CO_2R on Ag have not been studied in detail, especially concerning its product selectivity under different electrolyte environments. Meanwhile, numerous experimental and theoretical studies on other metals like Cu have shown that electrolyte

Received: February 26, 2026
Revised: May 6, 2026
Accepted: May 27, 2026

effects play key roles in tuning the local environment, intermediate stabilization, surface restructuring, and selectivity toward different products.[20−30] Monteiro et al. investigated the influence of the presence of electrolyte cations on CO_2R, finding that the reaction does not occur on Au, Ag, and Cu electrodes in the absence of alkali metal cations.[25] A CO_2R study on Ag investigated electrolyte effects with different cations and suggested that larger cations, such as K^+ or Cs^+, have a lower hydration effect, leading to stronger adsorption on the electrode surface, consequently stabilizing the CO* intermediate.[29] Besides the effects of cation identity, some studies have noted that electrolyte concentration can influence CO_2R selectivity. Kas et al. studied CO_2R performance on electrodeposited Cu nanoparticles using $KHCO_3$ concentrations ranging from 0.1 to 0.5 M. They found that increasing the electrolyte concentration increased H_2 and CH_4 production but decreased C_2H_4 selectivity. They attributed this shift to the higher buffer capacity, which maintains a less alkaline local pH, favoring CH_4 formation.[30] One study suggested that, by adjusting alkalinity via the KOH concentration and thereby tuning the hydronium influence, the CO_2R selectivity of Ag can be shifted from CO to formate ($HCOO^-$) via altering hydrogenation barriers toward the respective product.[26] Furthermore, long-term operation of Ag electrodes often leads to increased formation of undesired H_2 with decreased selectivity to CO, presenting challenges for the industrial applications of Ag electrodes. Noting this dynamic behavior and the observations that Ag can sometimes produce other products (H_2, formate, and hydrocarbons), identification of the precise origins of altered CO_2R selectivity on Ag remains an unsolved challenge.

Here, we investigate the sensitivity of Ag-catalyzed CO_2R to electrolyte concentration and purity. We demonstrate that unexpected CH_4 formation on Ag electrodes correlates with the presence of trace Cu contamination, an effect that can be amplified at elevated electrolyte concentrations. Through density functional theory (DFT) simulations, we identified the tensile strain and d-band center upshift on the Cu adatoms as possible phenomena responsible for strengthening CO binding and thus opening the methane pathway. Additionally, we elucidate how the commonly used H-cell configuration using a cation-exchange membrane induces dynamic changes in the electrolyte environment that influence selectivity.

■ RESULTS AND DISCUSSION

Electrolyte Concentration and Cu Impurity Effects on Ag-Catalyzed CO_2R

The following summarizes the main experimental conditions used herein, unless otherwise specified. Hand-polished Ag foils (99.998% purity) were used as working electrodes, potentials are reported as V vs Ag/AgCl (3 M) without *iR* compensation, and aqueous electrolytes were prepared using unpurified $KHCO_3$ of 99.95% purity (trace metals ≤5 ppm), with continuously bubbled CO_2 into a glass H-type cell with electrode compartments separated by a cation-exchange membrane (Nafion 115). Gas- and liquid chromatography were used to quantify the evolved products. Further experimental details are provided in Supporting Note 1 in the Supporting Information file.

To initially explore the potential-dependent selectivity at different electrolyte concentrations, we conducted CO_2R in 0.1, 0.5, and 1.0 M $KHCO_3$ solutions, using freshly prepared electrodes and electrolytes for each tested concentration, stepping the potential from low to high cathodic overpotential (−1.5 to −2.3 V vs Ag/AgCl). The measured rates of gaseous product formation (reported as partial current densities, j) as a function of time and applied potential are provided in Figure S1. These experiments revealed that simple, polished silver electrodes can produce significant CH_4, with selectivity sensitive to both applied potential and electrolyte concentration. As noted above, a few other studies reported observing CH_4 generation from Ag, typically attributed to the application of high overpotentials or nanostructured morphologies.[12] Here, we discovered that the electrolyte concentration may also play an important role. We therefore investigated electrolyte effects in more detail by conducting CO_2R in 0.1, 0.3, 0.5, 0.7, and 1.0 M $KHCO_3$ solutions, each run continuously for 3 h at −2.1 V vs Ag/AgCl (approx. −1.2 V vs the reversible hydrogen electrode, RHE; see Supporting Note 1, Figure S2, and Table S1 for details on pH and *iR* corrections). Gaseous products measured repeatedly during each experiment (Figure 1a−f) were averaged over the duration and combined with postrun liquid product measurements. Figure 1g summarizes the resulting trends in selectivity versus electrolyte concentration.

The major products (CO, H_2, CH_4, and $HCOO^-$) each showed unique concentration-dependent trends. The FE(CO) decreased with increasing electrolyte concentration, consistent with the conclusion of a recent multiscale theoretical study, which suggests that CO_2 mass-transport limitations become significant at high $KHCO_3$ concentrations and high overpotentials.[31] However, its partial current density j(CO) reveals that the rate of CO production varied only slightly across the conditions tested. Conversely, H_2 production (by both metrics) increased monotonically with electrolyte concentration, with a $j(H_2)$ slope similar to that of the total current density. The increase in $j(H_2)$ over time, along with the increase in the total current density, was found to closely correlate with increased electrolyte concentration over time, a result of K^+ crossover through the cation-exchange membrane (see Zheng et al. for a detailed study of this effect[32]). Further experiments on this topic and discussions are provided in Supplementary Note 2. Interestingly, the $j(CH_4)$ trend followed that of $j(H_2)$ quite closely for electrolyte concentrations of 0.1−0.5 M, before deviating at higher concentrations. Liquid product measurements revealed that formate ($HCOO^-$) was produced in significant quantities, also showing a dependence on electrolyte concentration across the lower range before plateauing at higher values. Trace amounts of C_2H_4 were also observed.

Our results show that both potential and electrolyte concentration affect the amount of CH_4 observed on Ag. However, since hydrocarbon production on Ag is rare, we investigated whether impurities played a role, as impurities are often known to strongly influence product selectivity.[33] We specifically looked for Cu, as it is known to catalyze CH_4 production, among numerous other products.[34] Several studies also demonstrated that ppm-level Cu could lead to significant CH_4 production, although no detailed explanation for such phenomenon was provided.[35,36] We therefore closely examined both the electrode and electrolyte by spectroscopic methods. X-ray photoelectron spectroscopy (XPS) of the Ag electrode surface showed no detectable Cu 2p signal either before or after CO_2R was conducted in unpurified 0.5 M $KHCO_3$ for 3 h (Figure S3). To examine the electrolyte for possible contamination, inductively coupled plasma−optical

https://doi.org/10.1021/acselectrochem.6c00077
ACS Electrochem. XXXX, XXX, XXX−XXX

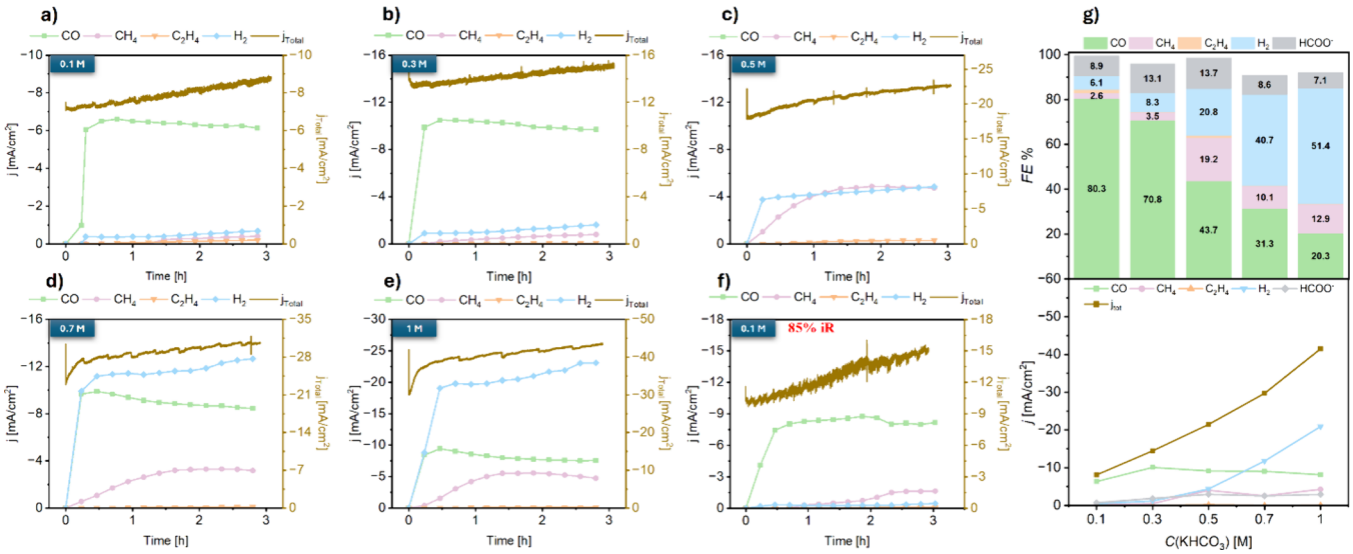

Figure 1. CO_2R product selectivity vs time for Ag foil electrodes tested at −2.1 V vs Ag/AgCl, reported as partial current densities (j) of gaseous products measured by online gas chromatography over 3 h in $KHCO_3$ electrolytes of concentrations (a) 0.1 M, (b) 0.3 M, (c) 0.5 M, (d) 0.7 M, and (e) 1 M $KHCO_3$ and (f) 0.1 M $KHCO_3$ with 85% iR compensation. (g) Summarized CO_2R product distribution shown as average Faradaic efficiencies (FE) and average partial current densities (j) over the 3 h duration. Experiments were conducted in unpurified aqueous $KHCO_3$ electrolytes of varying concentrations.

emission spectroscopy (ICP-OES) analysis was performed after electrolysis. As summarized in Table S3, three metallic impurities were detected, most prominently Cu, ranging between 1 and 13 μg/L (μg/L here equals to ppb, mass basis), but values below 2 μg/L were at or below the limit of precise quantification for the method (see Figure S21). Therefore, using this method, these contaminants are at the threshold of the detection limit. Thus, trace impurity levels are difficult to precisely quantify in solution and were not detectable on the electrode using surface-sensitive XPS.

Despite the trace nature of Cu impurities in solution, Cu atoms could gradually migrate and electrodeposit on the Ag working electrode under CO_2R conditions, accumulating on the catalytic surface and altering its selectivity. However, the challenging quantification of this trace amount of Cu hinders the identification of specific correlations between the electrode surface structure and selectivity. To better disentangle the factors contributing to CH_4 formation, we designed a set of experiments to precisely control the amount of Cu by first rigorously purifying the $KHCO_3$ electrolyte to remove heavy metal impurities, then adding controlled trace quantities of Cu, testing the activity of Ag electrodes under each condition.

Hereafter, all electrolytes were purified before use, using an ion-exchange resin (Chelex-100) to treat the aqueous $KHCO_3$ stock solutions, effective at reducing the Cu content to <1 μg/L (detailed in Supporting Note 1, quantified in Table S4). Subsequently, electrolytes with varying amounts of intentionally added Cu were tested (described below). Figure 2 presents the CO_2R selectivity of Ag as a function of electrolyte concentration and precisely controlled trace Cu content. Notably, in purified electrolytes (Figure 2a), CH_4 formation was no longer observed in significant amounts. The CO selectivity decreased with increasing $KHCO_3$ concentration, consistent with the conclusion of a recent multiscale theoretical study, which suggests that CO_2 mass-transport limitations become significant at high $KHCO_3$ concentrations and high overpotentials.[31] Interestingly, the FE of formate obtained from purified electrolytes remained largely unchanged compared to the unpurified case (Figure 1). These results suggest that the previous observations of CH_4 may be attributable to Cu impurities since reducing Cu below 1 μg/L suppresses CH_4 production to trace yields.

The influence of precise, trace amounts of Cu on the CO_2R performance of Ag was then examined by preparing electrolytes containing 2.5, 5, and 20 μg/L Cu (via addition of $CuSO_4$ followed by serial dilution). As shown in Figure 2a, in 0.1 M $KHCO_3$, only trace CH_4 was observed at Cu concentrations up to 5 μg/L. At the highest Cu concentration of 20 μg/L, the Faradaic efficiency and the partial current density (Figure S6) for CO decreased, accompanied by the emergence of additional C1 and C2 products. In more concentrated $KHCO_3$ (Figure 2b,c), CH_4 was formed as major CO_2R product across all tested conditions. Importantly, the presence of 2.5 μg/L Cu resulted in product distribution very similar to that observed in a 0.5 M unpurified electrolyte (Figure 1). This indicates that trace Cu, even as low as 2.5 μg/L, can disrupt the CO selectivity by promoting products beyond CO, and the effect is most prominent for $KHCO_3$ concentrations ≥0.5 M.

In the corresponding time-resolved selectivity data (shown in Figure S6), we observe that the $j(CH_4)$ begins low and increases gradually over time until it eventually stabilizes, a behavior that would be expected when resulting from the electrodeposition of trace solution species. Furthermore, the rate by which $j(CH_4)$ initially increases seems to scale directly with the concentration of added Cu, a trend likely governed by the different transport-limited deposition rates of Cu onto the electrode surface. The averaged rate of CH_4 formation as a function of both Cu concentration and $KHCO_3$ concentration across these experiments is summarized in Figure 2d. The trend of increasing $j(CH_4)$ with increasing $C(KHCO_3)$ is generally consistent with that observed on pure Cu by Resasco et al.[27] Its variation as a function of $C(Cu)$ suggests that the amount of Cu present may result in different Cu coverages on Ag under

https://doi.org/10.1021/acselectrochem.6c00077
ACS Electrochem. XXXX, XXX, XXX–XXX

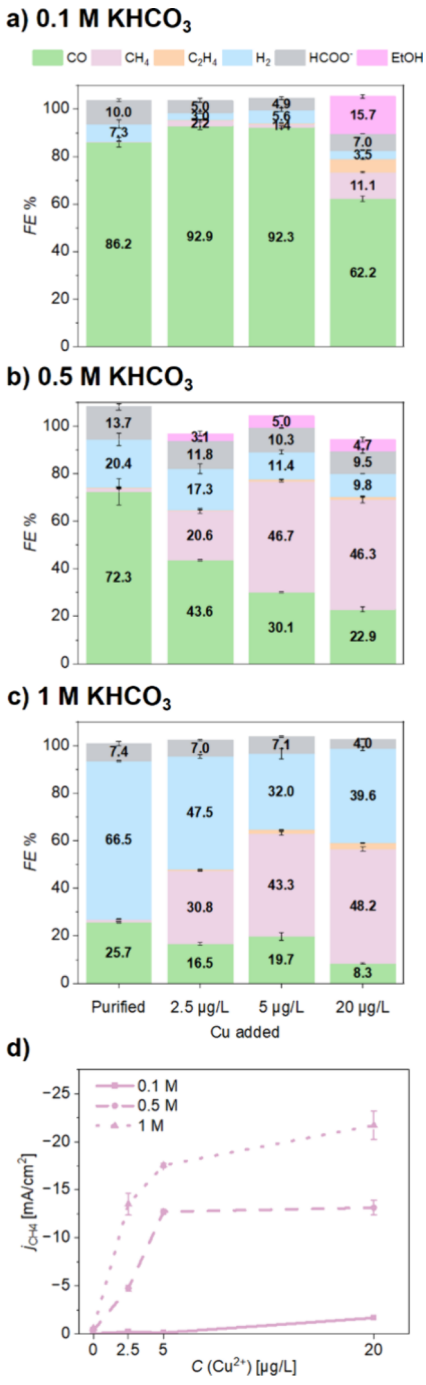

Figure 2. Product selectivity from CO_2R on Ag foil electrodes as a function of $KHCO_3$ concentration: (a) 0.1 M, (b) 0.5 M, and (c) 1 M; for purified electrolytes and electrolytes with various amounts of Cu added. (d) Summary of trends in $j(CH_4)$ versus $C(Cu^{2+})$ and $C(KHCO_3)$. Experiments were performed at $E_{Ag/AgCl} = -2.1$ V in CO_2-sparged electrolytes, two replicate times for every condition with each using a fresh electrode and electrolyte, with average values reported here (error bars represent standard deviations of the replicate experiments). The complete dataset is provided in Figure S6.

each condition. Further evidence of this comes from comparing the number of Ag surface atoms (based on the density and electrode surface area) and Cu atoms in the electrolyte, which reveals that a $C(Cu)$ of ca. 6.4 µg/L would provide sufficient Cu atoms for one monolayer coverage, if perfectly distributed on a pristine Ag surface. This could explain the apparent plateauing of CH_4 production when going to the higher $C(Cu)$ of 20 µg/L, although due to the dynamic nature of Cu impurity deposition (discussed in more detail below), we cannot know the precise structure of the deposited material. In Figure S5, we compare the CO_2R activity of this 20 µg/L Cu-doped case to that of bulk Cu (foil electrodes 99.9999% Cu, metal basis) in three concentrations of purified electrolytes. At low $C(KHCO_3)$, there are clear differences between the two, most notably that pure Cu produces significant C_2H_4 and negligible CO. At 1 M $KHCO_3$, however, the product selectivities appear to converge, with both producing mainly CH_4 and H_2. Hence, the selectivity of both Cu and Cu-contaminated Ag electrodes shows strong dependence on electrolyte concentration, but their differences indicate that some synergetic effects may be at play, which we discuss later in this study.

These observations suggest that Cu gradually electrodeposits onto the Ag working electrode, with both selectivity and its time dependence varying with the Cu concentration. This indicates that even ppb-level Cu can significantly change the product selectivity of Ag electrodes. However, difficulty in detecting and quantifying the adsorbed Cu makes it challenging to draw specific structure−activity correlations here. The inability to observe Cu by XPS might be due to the instability of the adsorbed Cu, which may detach from the Ag surface after the electrochemical experiments. We thus adapted the experimental procedure to improve retention of the electrodeposited species by maintaining the applied cathodic bias while withdrawing the electrode from solution following 2 h of CO_2R (to hopefully minimize Cu desorption), then transferring to the XPS system. Still, as shown in Figure 3a, no significant differences were observed among the spectra, and no pronounced Cu 2p signal was detected, except for the 20 µg/L Cu case where a very weak feature between 932−935 eV seems to appear. Therefore, adsorbed Cu may still be detaching from the surface before analysis, or the amount of Cu is simply too small to be clearly resolved by conventional XPS.

We then wondered whether an electrode initially activated in a solution containing trace Cu could retain its activity toward CH_4 even after transferring it to a purified, Cu-free electrolyte. We tested this by conducting 1.5 h of electrolysis in a solution containing 5 µg/L Cu, then withdrawing the electrode under an applied cathodic bias, replacing the electrolyte with fresh Chelex-purified solution, and then resuming CO_2R testing. As shown in Figure S10, significant $j(CH_4)$ was maintained after the exchange, suggesting that this approach may preserve adsorbed Cu on the Ag surface, thereby retaining CH_4 selectivity.

As discussed above, conventional analytical methods struggled to detect Cu either on the Ag surface or in solution, likely due to the detection limit of XPS and the weak adhesion of electrochemically deposited Cu. Nevertheless, the controlled addition of Cu to purified electrolytes clearly demonstrated that ultratrace Cu has a pronounced impact on product selectivity, which correlated with our observations in unpurified electrolytes. Seeking more direct in situ evidence of surface Cu accumulation, we employed electrochemical methods. While Cu can be electrodeposited cathodically, it can conversely be oxidized at more positive potentials, which would be signalled by anodic current.[37,38] We therefore assessed cyclic voltammetry (CV) responses obtained before and after CO_2R conducted in electrolytes with varying Cu contents, which revealed clear

https://doi.org/10.1021/acselectrochem.6c00077
ACS Electrochem. XXXX, XXX, XXX−XXX

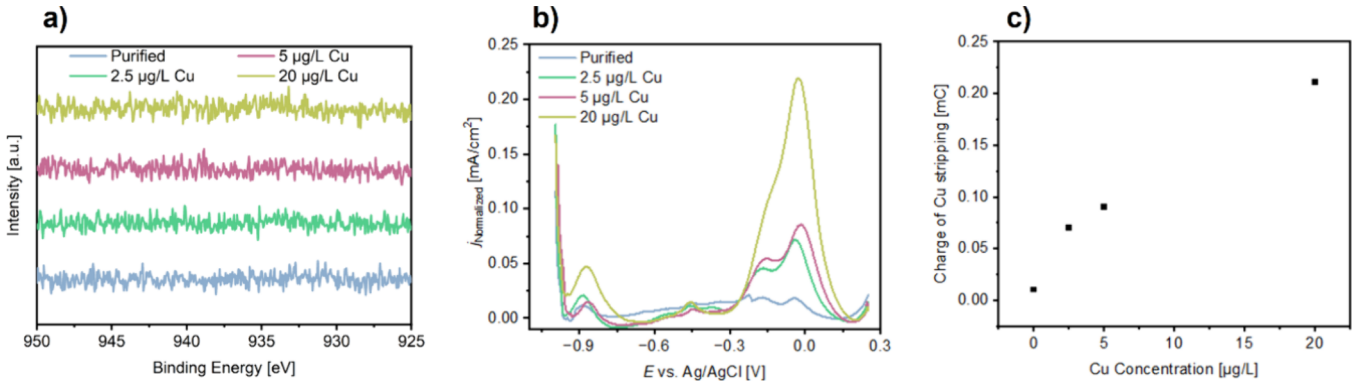

Figure 3. Surface characterization of Ag foil electrodes after CO_2R testing in purified 0.5 M $KHCO_3$ electrolytes with varied amounts of added Cu. (a) XPS spectra of Ag surfaces after CO_2R. Electrodes were withdrawn while maintaining −2.1 V applied bias aimed at avoiding Cu desorption. The Cu 2p peak is expected at a binding energy of 932.6 eV. (b) Baseline-normalized cyclic voltammograms (first anodic scan) directly after CO_2R testing in solutions of different Cu contents. (c) Correlation between the Cu concentration and the integrated charge of the stripping peak at ∼0 V vs Ag/AgCl from (b). All CVs acquired from the experiment sets from Figure 2. Datasets for other electrolyte concentrations are provided in Figure S11.

differences. As shown in Figure S8, the electrodes initially exhibited a reversible redox peak centered around −0.65 V. After 2 h of electrolysis, this feature largely disappeared whereas new peaks appeared at −0.9, −0.4, and 0 V. A previous study reported that peaks at $E_{Ag/AgCl} \approx -0.9$ and 0 V on a Ag rotating disk electrode could be attributed to deposition of impurity metals Zn and Cu, respectively, by comparison with XPS.[38] By comparing to CVs obtained after CO_2R in unpurified 0.5 M $KHCO_3$ (Figure S4) to those following the Cu-added experiments (Figure 3b and Figure S8), we observed similar peak features appearing at $E_{Ag/AgCl} \approx 0$ V, supporting the assignment of this peak to Cu stripping, providing evidence of Cu accumulation on the electrode surface under CO_2R conditions.

In Figure S8, there appears to be a correlation between the size of the Cu stripping peak and the Cu concentration of the electrolyte. To better visualize this trend, these CVs (conducted directly after 2 h of CO_2R) were normalized by background subtraction, and the anodic waves were compared across Cu amounts. A representative set of first anodic sweeps for 0.5 M $KHCO_3$ is shown in Figure 3b, and Figure 3c plots the corresponding integrated charge of the peaks around 0 V against the added Cu concentration (data for other concentrations are shown in Figure S11). The strong correlation suggests that anodic stripping can detect adsorbed Cu and reveal trends in relative amounts of Cu between experiments. We observed that Cu stripping features persist over multiple scans, gradually diminishing with each subsequent cycle (Figure S8). This contrasts with the previous work by Wuttig et al., which emphasized that their Cu stripping signal is detectable only during the first CV cycle.[38] A possible reason for the difference is our longer electrolysis period of 2−3 h (compared to only 45 min in their study), which likely resulted in a greater amount of Cu deposited on the Ag surface, making it persist over several CV scans.

We note that additional CV peaks are visible in our experiments. Some studies suggest that peaks at around −0.6 and −0.4 V could be related to anion-specific adsorption on distinct Ag facets,[10,39,40] which here may indicate that some surface restructuring occurs during our CO_2R studies, evidenced by the disappearance of the peak at −0.6 V and the appearance of a new peak at −0.4 V (even in Cu-free purified electrolytes, see Figure S8). Interestingly, only the peak at $E_{Ag/AgCl} \approx 0$ V correlated closely with rising Cu concentration across all three electrolytes. Meanwhile, another peak at −0.9 V was also observed, suggesting the presence of Zn impurities contributing to this feature. Indeed, the XPS spectra (Figure S7) indicated Zn on the electrode surface, particularly in the 5 and 20 μg/L cases, likely originating from the $CuSO_4$ stock solution, or contributing from the experimental setup, e.g., the current collector clip (the experimental setup is shown in Figure S17). The presence of Zn (and other trace metals) can also affect selectivity, and Zn is the only detectable impurity from XPS; thus, we examined its possible influence by conducting a spike experiment adding 10 μg/L $ZnCl_2$ to purified 0.5 M $KHCO_3$. The results are summarized in Figure S9. Compared to the behavior in a purified electrolyte, no clear differences were observed in the presence of Zn, suggesting that Ag-catalyzed CO_2R is largely insensitive to ppb-level Zn contamination. While our results identified Cu as a trace impurity capable of significantly altering the selectivity of Ag, real systems will likely contain multiple impurities, which could codeposit on the working electrode, and we therefore recommend that further studies investigate the effects of the presence of two or more impurity elements to look for potential synergetic effects.

Overall, our experiments showed how impurities (Figures 1 and 2) and electrolyte ions (Supplementary Note 2) can both be involved in dynamic processes which greatly influence product selectivity. To assess the effects over longer durations, we conducted a 10 h CO_2R experiment under conditions previously found to give prominent CH_4 (purified 0.5 M $KHCO_3$, doped with 5 μg/L Cu). As shown in Figure S22, after initially rising and stabilizing during the first 2 h, the CH_4 production rate steadily decreased over the remaining duration, while the H_2 yield steadily increased. Our aforementioned data showed how H_2 selectivity strongly and directly correlates with $KHCO_3$ electrolyte concentration (at the expense of other products), and we believe that this effect is dominating here as well due to ion crossover and the significant increase in concentration, which results on this timescale. The CH_4 activity significantly diminishing over this duration may signal that this electrolyte effect also acts to suppress CH_4, but we cannot rule out that the structure of the Cu adsorbed on Ag might be dynamic or unstable on this timescale due to the previously discussed challenges in observing the active catalytic interface.

https://doi.org/10.1021/acselectrochem.6c00077
ACS Electrochem. XXXX, XXX, XXX−XXX

More advanced methods to observe the electrode structure, such as in situ spectroscopy, could be useful for better understanding the interplay between the electrode structure and microenvironment effects. Furthermore, examining these ppb metal impurity effects under high-performance, scalable device configurations (e.g., using gas diffusion electrodes operating at higher current densities) will be important for assessing the practical significance of the phenomena we uncovered here.

Density Functional Theory Screening on Different Metal Substrates

Our experiments demonstrate that trace Cu alters the selectivity of Ag, leading to unexpected CH_4 production and raising the question of how such trace Cu can cause this drastic selectivity shift. On pristine copper, methane formation is expected to occur on (111) domains,[41] with CO protonation as the rate-determining step. Early studies by Nørskov and co-workers suggested *CHO to be the favorable intermediate, given its lower formation energy than *COH.[42,43] However, recently, a study by Abild-Pedersen and co-workers challenged this well-established notion, by proposing *CHO formation to be kinetically hindered.[44] From the catalytic point of view, Cu-based materials are the ideal choice for forming methane, given their mild *CO binding, while metals with a deeper d-band center, such as Ag and Au, are limited by CO desorption. Furthermore, pure Cu is highly selective for C_2H_4 formation, which is driven by its intrinsic ability to facilitate C−C coupling.[34] Importantly, while pure polycrystalline Cu typically shows high selectivity for C_2H_4, in our experiments, C_2H_4 was only a trace product. This suppression of C_2H_4 suggests that the active site is not merely bulk Cu, but rather, a Ag−Cu synergistic effect that promotes the C_1 pathway while hindering C_2 coupling.

Depositing monolayers of dopants on other transition metals is well-known to induce changes in the surface metal d-band centers.[45] Such a change may be partially due to compressive or tensile strain arising from lattice vector mismatch since tensile strain leads to an upshift of the d-band levels.[46] In turn, changes in the d-band centers directly influence the metal reactivity through the well-established d-band model.[47,48] Very recently, strain effects have been used to induce remarkable C_{2+} formation on Cu(0001)[49] and the opening of the ethanol pathway on distorted Cu domains,[50] among other findings.[51−53] Given the significant strain induced on a Cu monolayer if adsorbed on Ag, we hypothesize that the surface strain of electrodeposited Cu is a factor influencing methane formation on polycrystalline silver in the presence of electrodeposited Cu impurities.

We therefore conducted a model study of Cu layers deposited atop different transition metals, looking for trends influencing the CH_4 pathway. We carried out DFT simulations through the PBE density functional,[55] accounting for van der Waals interactions via the DFT-D2 method.[56,57] As structural models, we compared the effects of copper on several different transition metals, via a model of 4 layer-thick metal substrates (with the bottom two fixed to mimic bulk), Ni(111) p(3 × 3), Cu(111) p(3 × 3), Pd(111) p(3 × 3), Au(111) p(3 × 3), and Ag(111) p(3 × 3). We added 1 monolayer (ML) Cu on top of the substrates to mimic experimental results, where, based on impurity levels, electrolyte volume, and electrode area in our experiments, we estimate that complete electrodeposition of the Cu impurities present would result in an equivalent coverage on the order of one monolayer. We decided to expand the DFT screening beyond the sole Ag substrate to unveil potential trends among transition metals, while we chose the (111) facet as the preferential for methane formation[41] and most abundant in synthesized catalyst (polycrystalline silver). Figure 4a,b reports the top and side views of a typical model, expanded for clarity to a 9 × 9 supercell extension, while Figure 4c lists the d-band center of the simulated bulk transition metals, together with their lattice constant and lattice mismatch between the bulk metal substrate and Cu monolayer (as reported in Table 1).

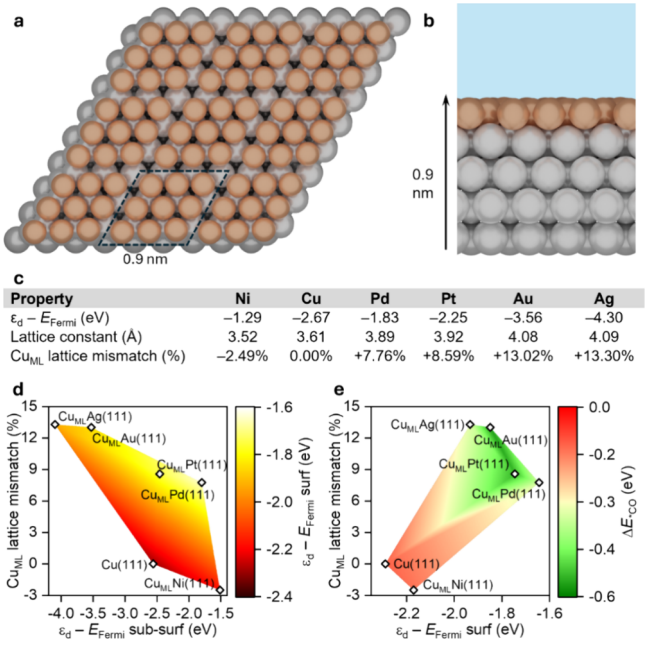

Figure 4. (a) Top and (b) side views of a typical $Cu_{ML}M(111)$ p(3 × 3) employed in the study (Cu = brown atoms; M = gray atoms), with M = Ni, Cu, Pd, Pt, Au, and Ag. In panel (a), the p(3 × 3) supercell is highlighted via dashed lines. (c) d-band centers vs Fermi energy and lattice constants of various transition metals.[45,54] Cu_{ML} lattice mismatch indicates the relative stretching/compression on 1 Cu ML when deposited on top of other metals (calculated vs Cu lattice constant). (d) Dependence of the d-band center of the Cu surface monolayer (color scale) vs the d-band center of the subsurface layer (*x*-axis) and lattice mismatch (*y*-axis). (e) CO formation energy (color scale) vs d-band center of the surface layer (*x*-axis) and lattice mismatch (*y*-axis).

In terms of electronic properties, we confirm a clear dependence between the d-band center of the Cu surface monolayer vs the d-band center of the subsurface layer (*x*-axis in Figure 4d) and the induced strain (lattice mismatch reported as the *y*-axis in Figure 4d; values reported in Table 1). Substrates that induce significant tensile strain on Cu (e.g., Ag and Au, see Figure 4c) result in an upshift of Cu d-band states beyond the value of bare Cu (−2.56 eV, see Table S5). A comparable trend is observed for metals with a lattice constant similar to Cu (e.g., Pd and Pt, see Figure 4c), but with a higher d-band center. In this case, the upshift of the Cu d-band center is due to electronic effects, in line with ref 45. Such an upshift, in turn, leads to a stronger binding of CO_2 reduction intermediates. In line with the d-band model,[47,48] the *CO formation energy decreases as the d-band center of surface Cu atoms increases (Figure S13), although this relationship is not strictly linear due to the strain induced by the substrate. Particularly, such a decrease is milder for substrates leading to compressive (Ni) or mild tensile strain (Pd and Pt), while Ag and Au, due to their high induced strain, determine very exothermic values

https://doi.org/10.1021/acselectrochem.6c00077
ACS Electrochem. XXXX, XXX, XXX−XXX

Table 1. d-Band Centers vs Fermi Energy and Lattice Constants of Various Transition Metals Retrieved, Respectively, from Ref 45 and Ref 54[a]

property	Ni	Cu	Pd	Pt	Au	Ag
$\varepsilon_d - E_{Fermi}$ (eV)	−1.29	−2.67	−1.83	−2.25	−3.56	−4.30
lattice constant (Å)	3.52	3.61	3.89	3.92	4.08	4.09
Cu_{ML} strain (%)	−2.49	0.00	+7.76	+8.59	+13.02	+13.30

[a]The Cu_{ML} strain indicates the relative stretching/compression on 1 Cu ML when deposited on top of other metals (calculated vs Cu lattice constant).

of ΔE_{*CO} (respectively −0.33 and −0.56 eV vs −0.12 eV for bare Cu, see Table S5). In fact, *CO formation energy depends linearly on both Cu surface atoms' d-band center and induced strain (Figure 4e and Table S6), as described in eq 1. We recall that the surface strain is here described by the lattice mismatch, reported in Figure 4c and calculated as the relative change of the lattice constant between pristine Cu and the metal (M) substrate. Such dependence is strongly affected by the d-band center ($b_1 = +0.35 \pm 0.07$), whereas it is only slightly dependent on lattice mismatch ($b_2 = +0.014 \pm 0.008$ eV/%). On one hand, an upshift (or downshift) of the d-band center vs the Cu reference value leads to a strengthening (or weakening) of CO binding. On the other hand, tensile (or compressive) strain induces a further strengthening (or weakening) of CO binding. $Cu_{ML}Ag(111)$ outperforms Cu(111) in terms of methane selectivity, owing to its stronger CO binding (−0.33 eV vs −0.12 eV), which prevents CO desorption and enables further protonation to *CHO. Due to this interplay between strain and electronic effects, we suggest that $Cu_{ML}Au(111)$ and $Cu_{ML}Pt(111)$ may surpass $Cu_{ML}Ag(111)$ regarding methane productivity, as both these substrates show the best trade-off between strain/d-band center (Figure 4e)

$$\Delta E_{*CO}\left(\varepsilon_d, \frac{\Delta d}{d}\right) = \Delta E^0_{*CO} - b_1\varepsilon_d - b_2\frac{d_{Cu} - d_{M_{sub}}}{d_{Cu}} \quad (1)$$

where d_{Cu} is the Cu lattice constant and $d_{M_{sub}}$ is the lattice constant of the metal substrate.

Similar correlation between formation energy, surface strain, and d-band center is expected for further intermediates (*CHO and *COCOH), given the existence of linear scaling relationships (LSR) between their formation energies and ΔE_{*CO} (Figure S12 and Table S7). Such LSRs are stronger for C-based intermediates, suggesting that *CHO and *COCOH formation are favored over *H formation, which motivates the limited hydrogen evolution observed in the experimental studies. While *CHO energy is endothermic for all the investigated substrates, *CO protonation to *CHO ($\Delta E_{*CHO} - \Delta E_{*CO}$, occurring via a proton-coupled electron transfer) requires low energy (<0.7 eV), which, according to the computational hydrogen electrode,[58] is easily achieved at a mild applied potential (−0.7 V vs RHE). Regarding C_{2+} products, their minimal detection is likely due to the significant energy demand required for stabilizing the rate-determining step formation of the *COCO dimer (>0.9 eV, see Table S5),[59] a precursor to *COCOH.

Given the polycrystalline nature of the experimental silver electrode, we investigated whether the postulated strain/d-band center effect on binding properties equally affected different surface facets. Thus, we complemented the initial study assessing *CO binding on additional (100), (110), and (211) p(3 × 3) facets on clean Ag and Cu surfaces and $Cu_{ML}Ag$ systems. The additional simulations confirmed an upshift of the d-band center of the Cu monolayer, which increases in magnitude depending on the tensile strain induced on Cu_{ML} (see Figure S15 and Table S9). Due to the peculiar step geometry of the (211) domain, compressive strain was observed in this case, causing, as hypothesized, a milder *CO binding than other domains, as observed for CuMLNi(111) (see Figure S15, Table S5, and Table S9).

As a final note, we investigated the possibility that the observed Cu concentration-dependent CH_4 selectivity arose due to partial coverage effects. By comparing the structural and electronic properties of $Cu_{ML}Ag(111)$ and $Cu_{2/3ML}Ag(111)$, we observed no significant changes in terms of the d-band center or surface strain (Figure S14 and Table S5). Rather than further expanding, the 2 × 2 Cu supercell adsorbed on the substrate remains an isolated island, at the cost of a higher formation energy (1.1 eV vs 0.6 eV for 1 ML, formation energy per unit atom, see Table S8). As a logical consequence, then, no significant changes in binding properties are observed. Thus, rather than motivating the correlation between methane productivity and Cu bulk concentration via coverage effects on binding properties, we suggest that mass transfer (faster deposition, since diffusion linearly depends on the concentration gradient) and increased density of active sites are the two factors potentially responsible for this effect. Given the mild endothermic formation energy for a full monolayer of Cu on Ag(111), i.e., 0.6 eV, we expect the deposition to be thermodynamically facile and easily reversible, in line with recent suggestions on Cu redeposition/dissolution cycles on Cu materials during operation.[60,61]

■ CONCLUSIONS

In summary, we employed a simple Ag foil H-cell CO_2R system and observed strong CH_4 formation, particularly under moderate or high $KHCO_3$ concentrations. Suspecting metal impurities as the culprit, we closely examined the electrolyte and electrode surface after CO_2R, failing to find clear evidence of contamination within the detection limits of conventional methods. However, upon rigorously purifying the $KHCO_3$ beforehand using ion-exchange resin to remove trace dissolved transition metals, CO_2R on Ag no longer yielded significant CH_4. Subsequently, we found that controlled addition of ppb amounts of dissolved Cu could restore this high selectivity toward CH_4 and furthermore found that postelectrolysis cyclic voltammetry could help identify the presence of trace electrodeposited Cu on the electrode. We therefore implicate metal impurities coming from the commercial electrolyte salt as the main factor enabling CH_4 evolution on Ag.

These findings suggest that ultratrace contaminants not detected by standard methods can nevertheless have a great impact on CO_2R catalyst activity and selectivity. This has possible implications for some previous studies, which observed hydrocarbon products on Ag and attributed the unique selectivity to other factors. More generally, such effects are likely to prove important in the operation of practical devices, where rigorous electrolyte purification is economically unfeasible, and where long-term operation will increase the accumulation of electrodeposited impurities. Besides Cu, metals such as Fe, Ti, and Ni are common contaminants, which should be carefully

https://doi.org/10.1021/acselectrochem.6c00077
ACS Electrochem. XXXX, XXX, XXX–XXX

assessed going forward. After a comprehensive examination, from a practical perspective, metal impurities that strongly perturb the system should be minimized from device manufactures, while developing catalysts with enhanced tolerance to such impurities represents an important direction. However, detailed technoeconomic analyses would be needed to assess which approach is most relevant for each application.

Since the high selectivity toward CH_4 we observed differs from the typical behavior of bulk Cu electrodes, we suspected that a synergetic effect between Ag and Cu leads to this unique behavior. We tested this by conducting DFT modeling on the properties of Cu monolayers atop Ag, which found that strain-induced shifts in the d-band center correlate to strengthened *CO adsorption (compared to pure Cu), thereby facilitating *CHO formation and opening the methane pathway. Extending this methodology to substrates of other transition metals with a shallow d-band center (Pd and Pt) or positive lattice mismatch with Cu (Au), we find a similar trend, which suggests that these metals can be similarly susceptible to such effects of Cu impurities. This trend may suggest an interesting general protocol to tune catalytic activity.

Finally, we observed a strong dependence of product selectivity on the electrolyte concentration. The most sensitive was the rate of H_2 formation, which scaled directly with $C(KHCO_3)$, whereas the CO formation rate was less variant. We identified that using cation-exchange membranes allows the facile transport of alkali cations as primary current-carrying ions, leading to continuous changes to electrolyte concentration over time, which correlated with selectivity changes. The use of an anion-exchange membranes could suppress cation crossover and improve the durability of the test. However, the loss of FE($HCOO^-$) due to anodic oxidation should be carefully considered. We conclude by emphasizing that these observations of trace impurity effects and of dynamic electrolyte composition were enabled by conducting experiments at sufficiently long durations where the effects could manifest, followed by careful examination of the system after the experiments by a variety of methods in order to understand the dynamic nature of the phenomena. These lessons may prove valuable for both fundamental studies of model systems as well as for practical devices under extended operation.

■ EXPERIMENTAL SECTION

Materials

For all experiments, Ag foil (0.25 mm thick, 99.998% Alfa Aesar) and Cu foil (0.25 mm thick, 99.9999% Thermo Scientific) were hand-polished separately using two polishing clothes (PSA Backing, Buehler) and alumina suspension in H_2O (0.05 μm Al_2O_3, Buehler) for 10 min to have a mirror-like surface. The foils after the polish were sonicated in a mixture of isopropanol and Milli-Q water (18.2 MΩ cm) for 10 min to remove the alumina and organic compounds. The $KHCO_3$ (≥99.95%, trace metal basis, Sigma-Aldrich) electrolyte solution was prepared in different concentrations with Milli-Q water and then used without any further purification unless otherwise specified. Electrolyte pH was measured by a pH meter (FiveEasy F20, Mettler Toledo).

For experiments labeled as "purified", the following additional protocols were followed for treating the electrode and electrolyte. The Ag foil was first immersed and etched in concentrated nitric acid (Honeywell, >65%), rinsed thoroughly with water, and then polished following the procedure described above. The electrolyte was purified using Chelex-100 resin (sodium form, 50−100 mesh, dry, Sigma-Aldrich), which was pretreated with slight modifications to the manufacturer's instructions and other publications.[62,63] Specifically, 100 g of resin was stirred in 1 L of 1 M HCl for 30 min to achieve protonation, then filtered, and washed with Milli-Q water until the effluent reached neutral pH. The resin was subsequently stirred in 1 L of 1 M KOH for 30 min, then filtered again, and washed with 2 L of Milli-Q water. This treatment can exchange Na^+ for K^+. ICP-OES analysis found that in purified 0.5 M $KHCO_3$, the residual Na^+ concentration was low, around 72.9 μM. Purification was performed using a batch method by adding 5 g of Chelex-100 resin to 500 mL of 1 M $KHCO_3$ and stirring for 2 h. The purified electrolyte was subsequently filtered to separate it from the Chelex solids. Lower electrolyte concentrations were prepared via dilution of this purified 1 M stock solution.

Electrolytes with intentionally added Cu were prepared using these Chelex-100-treated solutions of varied $KHCO_3$ concentration as stock solutions, adding 10 mM $CuSO_4{\cdot}5H_2O$, and then diluting with the same stock solutions to target a range of final Cu concentrations of 2.5−20 μg/L. A similar method was used to prepare a 0.5 M $KHCO_3$ with 10 μg/L $ZnCl_2$ electrolyte. These were measured by ICP-OES to determine the precise Cu and Zn levels.

Electrochemical Tests

The CO_2R experiments were all conducted in a two-compartment H-cell separated by a cation-exchange membrane (Nafion N-115, 0.125 mm thick, Alfa Aesar). A Ag/AgCl electrode (3 M KCl, PalmSens) and a Pt mesh with a high surface area were employed as reference and counter electrodes, respectively. Before each experiment, the Ag/AgCl was immersed in 3 M KCl solution, and the Pt mesh was immersed in concentrated nitric acid (65 wt %, Sigma-Aldrich), the H-cell was soaked in aqua regia for at least 30 min, rinsed with Milli-Q water, and sonicated to remove any trace metal impurities from the glass and ceramic gas distributor. Additionally, the Nafion membrane was soaked in 2 M H_2SO_4 and rinsed with purified $KHCO_3$.

The electrochemical experiments were conducted using a BioLogic SP-200 potentiostat. Before each experiment, the $KHCO_3$ electrolyte was presaturated with CO_2 (99.998%, Linde) and the CO_2 was continuously sparged through the electrolyte during the experiments with a flow rate of 20 mL/min, controlled by a mass flow controller (Red-Y GSC-A9TA-BB21). The electrochemical experiments were performed using the following sequence:

1. Open-circuit potential (OCP) for 3 min.
2. Cyclic voltammetry (CV) from −1.0 to 0.25 V vs Ag/AgCl with a scan rate of 200 mV/s, repeated for 20 cycles.
3. Potentio electrochemical impedance spectroscopy (PEIS) at a DC potential of −1.51 V vs Ag/AgCl. Amplitude, 10 mV; frequency range, 200 kHz to 100 mHz.
4. R_u measured at 200 kHz (automatic *iR* compensation was not applied, unless otherwise stated).
5. Chronoamperometry (CA) was conducted for 3 h. For stepped-potential experiments, each potential was maintained for 1 h.
6. Repeat (2) and (3).

Gaseous products were analyzed by in-line gas chromatography (GC, Thermo Scientific Trace 1310/1300) equipped with a pulse discharge detector (PDD) and flame ionization detector (FID). Injections took place every ∼15 min. The partial current density *j* and Faradaic efficiency FE per product *i* were calculated with eqs 2 and 3 below, respectively:

$$j_i = \frac{\dot{V} \times C_i \times z_i \times F}{R \times T} \tag{2}$$

$$\mathrm{FE}_i = \frac{j_i}{j_{\mathrm{total}}} \times 100\% \tag{3}$$

where $\dot{V}$ is the CO_2 flow rate, C_i is the measured concentration of species *i* determined by GC, z_i is the number of electrons transferred

https://doi.org/10.1021/acselectrochem.6c00077
ACS Electrochem. XXXX, XXX, XXX−XXX

to form 1 mol of gaseous species i, F is the Faraday constant 96,485 C/mol, R is the molar gas constant 8.314 m^3 Pa/K mol, T is the temperature 298 K, and j_{total} is the total current measured by the potentiostat at the time of gas injection to the GC.

To quantify liquid products, ultrahigh-performance liquid chromatography (Thermo Scientific Model HPLC+ UltiMate 3000 series) was employed with UV-variable wavelength (UltiMate 3000, Dionex) and refraction index (RefractoMax 520, ERC) detectors and a HyperREZ XP H+ column. The evaluation of $HCOO^-$ was followed by eq 4:

$$FE = \frac{C_{HCOO^-} \times V \times z \times F}{Q_{total}} \times 100\% \quad (4)$$

where C_{HCOO^-} is the concentration of formate measured from HPLC, V is the volume of the electrolyte in the cell (25 mL), z is the number of electrons transferred to form 1 mol of formate (2 e^-), and Q_{total} is the total charge passed through the cell during the experiment duration.

Throughout the study, the sums of FEs for all products approach 100%, suggesting good accounting of mass balance in these experiments, within the standards common in the CO_2R field.[64] Minor observed deviations could result from a few factors such as the actual gas flow rate reaching the GC deviates from the V (due to conversion of CO_2 to liquid products and water electrolysis to generate H_2 gas), slightly affecting the gas dilution factor; the slight increase in the catholyte volume (ΔV_{cat} in Table S2, but not measured in every experiment) can affect liquid dilution, leading to underestimated FEs; reoxidation of liquid products at the anode can decrease their levels in solution. In H-cell experiments, each of these factors likely plays minor roles, but their combination may explain deviations from 100% FE sums.

Inductively Coupled Plasma–Optical Emission Spectroscopy (ICP-OES)

For the determination of K^+ concentration: A single-element ICP standard solution with potassium (1000 mg/L K^+ in 2% HNO_3, Carl Roth) was diluted from 100 to 4000 μg/L as the calibration standards. The electrolyte sample was diluted 10,000 times with 2% HNO_3 in order to fit in the calibration range. The concentration of K^+ in the catholyte after each experiment was measured by an iCAP7400 Duo MFC ICP-OES analyzer (Thermo Scientific) in axial Ar plasma mode.

For the determination of Cu impurity: An ICP-OES multielement standard solution containing 23 elements (1000 mg L^{-1} of Cu, Ag, Fe, Ni, etc., in 6.5% HNO_3; Merck) was diluted with Milli-Q water to prepare calibration standards ranging from 1 to 100 μg L^{-1}. Electrolyte samples collected after experiments were measured directly by ICP-OES without further dilution, following the procedure described above, to detect the possible impurities from the electrolyte. The precision of ICP-OES becomes limited for impurity detection at Cu concentrations below 2 μg/L. As shown in Figure S20, the error bars from triplicate measurements are relatively large in this concentration range, indicating the reduced reliability of ICP-OES for quantifying Cu at very low concentrations.

X-ray Photoelectron Spectroscopy (XPS)

For surface analysis after experiments with unpurified electrolytes, XPS was performed directly on the Ag foils following the complete electrochemical sequence. For tests with defined Cu concentrations, ex situ XPS was employed as a surface-sensitive technique to probe the Ag surface composition. Measurements were conducted on freshly polished and post-electrolyzed Ag foils in different electrolyte conditions. To minimize the risk of Cu stripping from postrun cyclic voltammetry or potential interruptions, the electrodes were withdrawn from the electrolyte under an applied potential of −2.1 V, rinsed with Milli-Q water droplets to remove residual electrolyte, dried under ambient conditions, and immediately analyzed by XPS (SPECS PHOIBOS 100 analyzer, Al Kα source, 1486.74 eV).

Computational Details

We carried out the density functional theory by means of the Vienna ab initio simulation package (VASP)[65,66] through the PBE density functional.[55] To account for van der Waals interactions, we included dispersion through the DFT-D2 method,[56,57] with the parametrization of C6 coefficients for metals reported in ref 67. Inner electrons were represented by PAW pseudopotentials,[68,69] and the monoelectronic states for the valence electrons expanded as plane waves with a kinetic energy cutoff of 450 eV.

The experimental catalyst (polycrystalline silver foil) was modeled as a Ag(111) p(3 × 3) supercell (Figure 4a,b). Such a cell included at least four layers, with the two uppermost fully relaxed to resemble the surface and the rest fixed to the bulk distances. Besides this model, further substrates were Ni(111) p(3 × 3), Cu(111) p(3 × 3), Pd(111) p(3 × 3), Au(111) p(3 × 3), and Ag(111) p(3 × 3). All the employed models were generated via the Atomic Simulation Environment.[70] On each surface, a Cu monolayer was deposited on top with an analogous lattice constant as the underlying substrate and let to relax via full ionic optimization. For the Cu coverage study, we removed 5 atoms from the $Cu_{ML}Ag(111)$ structure, leading to a 2/3 ML Cu coverage. We sampled the Brillouin zone by a Γ-centered k-point mesh from the Monkhorst–Pack method,[71] with a reciprocal grid size smaller than 0.03 $Å^{-1}$. We set a vacuum thickness between the slabs larger than 12 Å to prevent spurious periodic interactions between periodic repetitions of the cells. Adsorbates (*CO, *CHO, *COCOH, and *H) were placed on atop sites only on one side of the slab; thus, we introduced a dipole correction during the simulation to account for artificial contributions from the asymmetric slab model.[72] All energies were reported using as a reference the surfaces and the energy of gas-phase CO_2, H_2, and H_2O. When required, the relative energy between the H^+ and the H_2(g) at $U = 0$ V was obtained with the computational hydrogen electrode.[58,73]

■ ASSOCIATED CONTENT

Data Availability Statement

The datasets generated through DFT simulations and analyzed during the current study are available in the ioChem-BD database[73] at DOI: 10.19061/iochem-bd-1-417. Experimental data sets are available from the corresponding author upon reasonable request.

Supporting Information

The Supporting Information is available free of charge at https://pubs.acs.org/doi/10.1021/acselectrochem.6c00077.

Detailed experimental procedures and methodologies, materials and their treatments, additional figures and tables referenced in the main text, including electrochemical characterization, product analysis, details of trace species analysis, and supplements to the DFT analysis (PDF)

■ AUTHOR INFORMATION

Corresponding Author

Matthew T. Mayer – *Electrochemical Conversion, Helmholtz-Zentrum Berlin für Materialien und Energie GmbH, Hahn-Meitner Platz 1, Berlin 14109, Germany;* orcid.org/0000-0001-5379-2775; Email: m.mayer@helmholtz-berlin.de

Authors

Chaoqun Ma – *Electrochemical Conversion, Helmholtz-Zentrum Berlin für Materialien und Energie GmbH, Hahn-Meitner Platz 1, Berlin 14109, Germany; Institute für*

https://doi.org/10.1021/acselectrochem.6c00077
ACS Electrochem. XXXX, XXX, XXX–XXX

Chemie und Biochemie, Freie Universität Berlin, Berlin 14195, Germany; orcid.org/0009-0004-2481-4380

Flora Haun – *Electrochemical Conversion, Helmholtz-Zentrum Berlin für Materialien und Energie GmbH, Hahn-Meitner Platz 1, Berlin 14109, Germany; Institute für Chemie und Biochemie, Freie Universität Berlin, Berlin 14195, Germany*

Federico Dattila – *CREST Group, Department of Applied Science and Technology (DISAT), Politecnico di Torino, Corso Duca degli Abruzzi 24, Turin 10129, Italy*; orcid.org/0000-0001-8195-3951

Wankai Tang – *Electrochemical Conversion, Helmholtz-Zentrum Berlin für Materialien und Energie GmbH, Hahn-Meitner Platz 1, Berlin 14109, Germany; Institute für Chemie und Biochemie, Freie Universität Berlin, Berlin 14195, Germany*

Gumaa A. El-Nagar – *Electrochemical Conversion, Helmholtz-Zentrum Berlin für Materialien und Energie GmbH, Hahn-Meitner Platz 1, Berlin 14109, Germany*; orcid.org/0000-0001-8209-4597

Ajin Anilkumar – *Electrochemical Conversion, Helmholtz-Zentrum Berlin für Materialien und Energie GmbH, Hahn-Meitner Platz 1, Berlin 14109, Germany; Institute für Chemie und Biochemie, Freie Universität Berlin, Berlin 14195, Germany*

Simelys Hernández – *CREST Group, Department of Applied Science and Technology (DISAT), Politecnico di Torino, Corso Duca degli Abruzzi 24, Turin 10129, Italy*; orcid.org/0000-0002-6722-0273

Complete contact information is available at: https://pubs.acs.org/doi/10.1021/acselectrochem.6c00077

Author Contributions

C.M., M.T.M., and G.A.E.-N. planned the study. C.M. performed the experiments and data analysis and drafted the manuscript. F.D. carried out the computational calculations and discussed the results. F.H. conducted and analyzed ICP-OES measurements. W.T and A.A. contributed to electrochemical experiments. All authors read and commented on the manuscript and approved the final version.

Funding

This work was funded by the Deutsche Forschungsgemeinschaft (DFG, German Research Foundation, project numbers 501805371 and 428712064) and the European Union's Horizon Europe research and innovation program under the Marie Sklodowska-Curie grant agreement no. 101104004 (SuPERCO2). F.D. and S.H. acknowledge the CINECA award under the ISCRA initiative, for the availability of high-performance computing resources and support.

Notes

The authors declare no competing financial interest.

■ ACKNOWLEDGMENTS

The authors thank Dr. Christian Höhn for assistance with XPS measurements. We acknowledge Ranga Rohit Seemakurthi for preliminary DFT calculations and early discussions regarding reaction mechanisms. We also appreciate Siddharth Gupta for fruitful discussions and valuable insights into experimental design. The authors used Gemini 3 to improve the language and readability of this manuscript. The authors reviewed and edited the content as needed and take full responsibility for the publication's content.

■ REFERENCES

(1) Sun, D.; Xu, X.; Qin, Y.; Jiang, S. P.; Shao, Z. Rational Design of Ag-Based Catalysts for the Electrochemical CO_2 Reduction to CO: A Review. *ChemSusChem* **2020**, *13* (1), 39−58.

(2) Masel, R. I.; Liu, Z.; Yang, H.; Kaczur, J. J.; Carrillo, D.; Ren, S.; Salvatore, D.; Berlinguette, C. P. An industrial perspective on catalysts for low-temperature CO_2 electrolysis. *Nat. Nanotechnol.* **2021**, *16* (2), 118−128.

(3) Augustynski, R. K.; Augustynski, J. Electrochemical Reduction of CO_2 at an Activated Silver Electrode. *Ber. Bunsenges. Phys. Chem* **1994**, *98* (12), 1510−1515.

(4) Hatsukade, T.; Kuhl, K. P.; Cave, E. R.; Abram, D. N.; Jaramillo, T. F. Insights into the electrocatalytic reduction of CO_2 on metallic silver surfaces. *Phys. Chem. Chem. Phys.* **2014**, *16* (27), 13814−13819.

(5) Chen, X.; Lu, R.; Li, C.; Luo, W.; Yu, R.; Zhu, J.; Lv, L.; Dai, Y.; Gong, S.; Zhou, Y.; et al. Activating inert non-defect sites in Bi catalysts using tensile strain engineering for highly active CO_2 electroreduction. *Nat. Commun.* **2025**, *16* (1), No. 1927.

(6) Lv, L.; Lu, R.; Zhu, J.; Yu, R.; Zhang, W.; Cui, E.; Chen, X.; Dai, Y.; Cui, L.; Li, J.; et al. Coordinating the Edge Defects of Bismuth with Sulfur for Enhanced CO_2 Electroreduction to Formate. *Angew. Chem., Int. Ed.* **2023**, *62* (25), No. e202303117.

(7) Zhu, J.; Li, J.; Lu, R.; Yu, R.; Zhao, S.; Li, C.; Lv, L.; Xia, L.; Chen, X.; Cai, W.; et al. Surface passivation for highly active, selective, stable, and scalable CO_2 electroreduction. *Nat. Commun.* **2023**, *14* (1), No. 4670.

(8) Singh, M. R.; Goodpaster, J. D.; Weber, A. Z.; Head-Gordon, M.; Bell, A. T. Mechanistic insights into electrochemical reduction of CO_2 over Ag using density functional theory and transport models. *Proc. Natl. Acad. Sci.* **2017**, *114* (42), E8812−E8821.

(9) Dorner, I.; Röse, P.; Krewer, U. Dynamic vs. Stationary Analysis of Electrochemical Carbon Dioxide Reduction: Profound Differences in Local States. *ChemElectroChem* **2023**, *10* (24), No. e202300387.

(10) Hoshi, N.; Kato, M.; Hori, Y. Electrochemical reduction of CO2 on single crystal electrodes of silver Ag(111), Ag(100) and Ag(110). *J. Electroanal. Chem.* **1997**, *440* (1), 283−286.

(11) Clark, E. L.; Ringe, S.; Tang, M.; Walton, A.; Hahn, C.; Jaramillo, T. F.; Chan, K.; Bell, A. T. Influence of Atomic Surface Structure on the Activity of Ag for the Electrochemical Reduction of CO_2 to CO. *ACS Catal.* **2019**, *9* (5), 4006−4014.

(12) Dutta, A.; Morstein, C. E.; Rahaman, M.; Cedeño López, A.; Broekmann, P. Beyond Copper in CO_2 Electrolysis: Effective Hydrocarbon Production on Silver-Nanofoam Catalysts. *ACS Catal.* **2018**, *8* (9), 8357−8368.

(13) He, Z.; Liu, T.; Tang, J.; Zhou, C.; Wen, L.; Chen, J.; Song, S. Highly active, selective and stable electroreduction of carbon dioxide to carbon monoxide on a silver catalyst with truncated hexagonal bipyramidal shape. *Electrochim. Acta* **2016**, *222*, 1234−1242.

(14) Rosen, J.; Hutchings, G. S.; Lu, Q.; Rivera, S.; Zhou, Y.; Vlachos, D. G.; Jiao, F. Mechanistic Insights into the Electrochemical Reduction of CO_2 to CO on Nanostructured Ag Surfaces. *ACS Catal.* **2015**, *5* (7), 4293−4299.

(15) Krause, R.; Reinisch, D.; Reller, C.; Eckert, H.; Hartmann, D.; Taroata, D.; Wiesner-Fleischer, K.; Bulan, A.; Lueken, A.; Schmid, G. Industrial Application Aspects of the Electrochemical Reduction of CO_2 to CO in Aqueous Electrolyte. *Chem. Ing. Tech.* **2020**, *92* (1-2), 53−61.

(16) Chen, C.; Khosrowabadi Kotyk, J. F.; Sheehan, S. W. Progress toward Commercial Application of Electrochemical Carbon Dioxide Reduction. *Chem* **2018**, *4* (11), 2571−2586.

(17) Varhade, S.; Guruji, A.; Singh, C.; Cicero, G.; García-Melchor, M.; Helsen, J.; Pant, D. Electrochemical CO_2 Reduction: Commercial Innovations and Prospects. *ChemElectroChem* **2024**, *12* (2), No. e202400512.

(18) Raaijman, S. J.; Schellekens, M. P.; Corbett, P. J.; Koper, M. T. M. High-Pressure CO Electroreduction at Silver Produces Ethanol and Propanol. *Angew. Chem., Int. Ed.* **2021**, *60* (40), 21732−21736.
(19) Shiratsuchi, R.; Nogami, G. Pulsed Electroreduction of CO_2 on Silver Electrodes. *J. Electrochem. Soc.* **1996**, *143* (2), No. 582.
(20) Zhang, Z.-M.; Wang, T.; Cai, Y.-C.; Li, X.-Y.; Ye, J.-Y.; Zhou, Y.; Tian, N.; Zhou, Z.-Y.; Sun, S.-G. Probing electrolyte effects on cation-enhanced CO_2 reduction on copper in acidic media. *Nat. Catal.* **2024**, *7*, 807−817.
(21) Liu, S.; Li, Y.; Wang, D.; Xi, S.; Xu, H.; Wang, Y.; Li, X.; Zang, W.; Liu, W.; Su, M.; et al. Alkali cation-induced cathodic corrosion in Cu electrocatalysts. *Nat. Commun.* **2024**, *15* (1), No. 5080.
(22) Wang, J.; Qin, Y.; Jin, S.; Yang, Y.; Zhu, J.; Li, X.; Lv, X.; Fu, J.; Hong, Z.; Su, Y.; et al. Customizing CO_2 Electroreduction by Pulse-Induced Anion Enrichment. *J. Am. Chem. Soc.* **2023**, *145* (48), 26213−26221.
(23) Monteiro, M. C. O.; Dattila, F.; Lopez, N.; Koper, M. T. M. The Role of Cation Acidity on the Competition between Hydrogen Evolution and CO_2 Reduction on Gold Electrodes. *J. Am. Chem. Soc.* **2022**, *144* (4), 1589−1602.
(24) Monteiro, M. C. O.; Goyal, A.; Moerland, P.; Koper, M. T. M. Understanding Cation Trends for Hydrogen Evolution on Platinum and Gold Electrodes in Alkaline Media. *ACS Catal.* **2021**, *11* (23), 14328−14335.
(25) Monteiro, M. C. O.; Dattila, F.; Hagedoorn, B.; García-Muelas, R.; López, N.; Koper, M. T. M. Absence of CO electroreduction on copper, gold and silver electrodes without metal cations in solution. *Nat. Catal.* **2021**, *4* (8), 654−662.
(26) Seifitokaldani, A.; Gabardo, M. C.; Burdyny, T.; Dinh, C.-T.; Edwards, P. J.; Kibria, G. M.; Bushuyev, S. O.; Kelley, O. S.; Sinton, D.; Sargent, H. E. Hydronium-Induced Switching between CO_2 Electroreduction Pathways.*J. Am. Chem. Soc.* **2018**, *140* (11), 3833−3837.
(27) Resasco, J.; Lum, Y.; Clark, E.; Zeledon, J. Z.; Bell, A. T. Effects of Anion Identity and Concentration on Electrochemical Reduction of CO. *ChemElectroChem* **2018**, *5* (7), 1064−1072.
(28) Zhong, H.; Fujii, K.; Nakano, Y. Effect of KHCO3 Concentration on Electrochemical Reduction of CO_2on Copper Electrode. *J. Electrochem. Soc.* **2017**, *164* (9), F923−F927.
(29) Michael, R.; Thorson, K. I. S.; Paul J. A. Kenis Effect of Cations on the Electrochemical Conversion of CO2 to CO. *J. Electrochem. Soc.* **2013**, *160* (1), F68−F74.
(30) Kas, R.; Kortlever, R.; Yilmaz, H.; Koper, M. T. M.; Mul, G. Manipulating the Hydrocarbon Selectivity of Copper Nanoparticles in CO Electroreduction by Process Conditions. *ChemElectroChem* **2015**, *2* (3), 354−358.
(31) Lorenzutti, F.; Seemakurthi, R. R.; Johnson, E. F.; Morandi, S.; Nikačević, P.; López, N.; Haussener, S. Microenvironment effects in electrochemical CO_2 reduction from first-principles multiscale modelling. *Nat. Catal.* **2025**, *8* (9), 905−918.
(32) Zheng, Z.; Yao, Y.; Yan, W.; Bu, H.; Huang, J.; Ma, M. Mechanistic Insights into the Abrupt Change of Electrolyte in CO_2 Electroreduction. *ACS Catal.* **2024**, *14* (8), 6328−6338.
(33) Yap, K. M. K.; Rodríguez Pabón, M.; Matthews, J. E.; Lee, S.-W.; Nielander, A. C.; Jaramillo, T. F. The Influence of ppm-Level Divalent Ionic Impurities from Real-World Feedstocks on Electrochemical Cu-Based CO_2 Reduction. *ACS Electrochem.* **2026**, *2* (4), 955−963.
(34) Nitopi, S.; Bertheussen, E.; Scott, S. B.; Liu, X.; Engstfeld, A. K.; Horch, S.; Seger, B.; Stephens, I. E. L.; Chan, K.; Hahn, C.; et al. Progress and Perspectives of Electrochemical CO_2 Reduction on Copper in Aqueous Electrolyte. *Chem. Rev.* **2019**, *119* (12), 7610−7672.
(35) Senocrate, A.; Bernasconi, F.; Rentsch, D.; Kraft, K.; Trottmann, M.; Wichser, A.; Bleiner, D.; Battaglia, C. Importance of Substrate Pore Size and Wetting Behavior in Gas Diffusion Electrodes for CO_2 Reduction. *ACS Appl. Energy Mater.* **2022**, *5* (11), 14504−14512.
(36) Gao, G.; Khiarak, B. N.; Liu, H.; Trần-Phú, T.; Obasanjo, C. A.; Crane, J.; Lai, H. D. T.; da Silva, G. T. S. T.; Golovanova, V.; Li, J.; et al. Recoverable operation strategy for selective and stable electrochemical carbon dioxide reduction to methane. *Nat. Energy* **2025**, *10* (11), 1360−1370.
(37) Cui, Z.; Marx, M. A.; Tegomoh, M. N.; Co, A. C. A Guide to Evaluate Electrolyte Purity for CO_2 Reduction Studies. *ACS Energy Lett.* **2023**, *8* (12), 5201−5205.
(38) Wuttig, A.; Surendranath, Y. Impurity Ion Complexation Enhances Carbon Dioxide Reduction Catalysis. *ACS Catal.* **2015**, *5* (7), 4479−4484.
(39) Stevenson, K. J.; Gao, X.; W. Hatchett, D.; White, H. S. Voltammetric measurement of anion adsorption on Ag(111). *J. Electroanal. Chem.* **1998**, *447* (1), 43−51.
(40) Huang, J.-F.; Wu, Y.-C. Tunable Ag Micromorphologies Show High Activities for Electrochemical H2 Evolution and CO_2 Electrochemical Reduction. *ACS Sustainable Chem. Eng.* **2019**, *7* (6), 6352−6359.
(41) Bagger, A.; Ju, W.; Varela, A. S.; Strasser, P.; Rossmeisl, J. Electrochemical CO_2 Reduction: Classifying Cu Facets. *ACS Catal.* **2019**, *9* (9), 7894−7899.
(42) Peterson, A. A.; Abild-Pedersen, F.; Studt, F.; Rossmeisl, J.; Nørskov, J. K. How copper catalyzes the electroreduction of carbon dioxide into hydrocarbon fuels. *Energy Environ. Sci.* **2010**, *3* (9), No. 1311.
(43) Peterson, A. A.; Nørskov, J. K. Activity Descriptors for CO_2 Electroreduction to Methane on Transition-Metal Catalysts. *J. Phys. Chem. Lett.* **2012**, *3* (2), 251−258.
(44) Peng, H.; Tang, M. T.; Liu, X.; Schlexer Lamoureux, P.; Bajdich, M.; Abild-Pedersen, F. The role of atomic carbon in directing electrochemical CO(2) reduction to multicarbon products. *Energy Environ. Sci.* **2021**, *14* (1), 473−482.
(45) Ruban, A.; Hammer, B.; Stoltze, P.; Skriver, H. L.; Nørskov, J. K. Surface electronic structure and reactivity of transition and noble metals. Communication presented at the First Francqui Colloquium, Brussels, 19−20 February 1996.1. *J. Mol. Catal. A: Chem.* **1997**, *115* (3), 421−429.
(46) Mavrikakis, M.; Hammer, B.; Nørskov, J. K. Effect of Strain on the Reactivity of Metal Surfaces. *Phys. Rev. Lett.* **1998**, *81* (13), 2819−2822.
(47) Hammer, B.; Nørskov, J. K. Electronic factors determining the reactivity of metal surfaces. *Surf. Sci.* **1995**, *343* (3), 211−220.
(48) Hammer, B.; Morikawa, Y.; Nørskov, J. K. CO Chemisorption at Metal Surfaces and Overlayers. *Phys. Rev. Lett.* **1996**, *76* (12), 2141−2144.
(49) Kim, T.; Kumar, R. E.; Brock, J. A.; Fullerton, E. E.; Fenning, D. P. How Strain Alters CO_2 Electroreduction on Model Cu(001) Surfaces. *ACS Catal.* **2021**, *11* (11), 6662−6671.
(50) Zhan, C.; Dattila, F.; Rettenmaier, C.; Herzog, A.; Herran, M.; Wagner, T.; Scholten, F.; Bergmann, A.; Lopez, N.; Roldan Cuenya, B. Key intermediates and Cu active sites for CO_2 electroreduction to ethylene and ethanol. *Nat. Energy* **2024**, *9* (12), 1485−1496.
(51) Sandberg, R. B.; Montoya, J. H.; Chan, K.; Nørskov, J. K. CO-CO coupling on Cu facets: Coverage, strain and field effects. *Surf. Sci.* **2016**, *654*, 56−62.
(52) Fan, Q.; Yan, P.; Liu, F.; Xu, Z.; Liang, P.; Cao, X.; Ye, C.; Liu, M.; Zhao, L.; Ren, S.; et al. Compressive strain in Cu catalysts: Enhancing generation of C_{2+} products in electrochemical CO_2 reduction. *Sci. Bull.* **2024**, *69* (18), 2881−2891.
(53) Niu, W.; Feng, J.; Chen, J.; Deng, L.; Guo, W.; Li, H.; Zhang, L.; Li, Y.; Zhang, B. High-efficiency C(3) electrosynthesis on a lattice-strain-stabilized nitrogen-doped Cu surface. *Nat. Commun.* **2024**, *15* (1), No. 7070.
(54) Misra, P. K.; Prasanta, K. Basic properties of crystals. *Phys. Condens. Matter* **2012**, 1−35.
(55) Perdew, J. P.; Burke, K.; Ernzerhof, M. Generalized Gradient Approximation Made Simple. *Phys. Rev. Lett.* **1996**, *77* (18), 3865−3868.
(56) Grimme, S. Semiempirical GGA-type density functional constructed with a long-range dispersion correction. *J. Comput. Chem.* **2006**, *27* (15), 1787−1799.
(57) Bučko, T.; Hafner, J.; Lebègue, S.; Ángyán, J. G. Improved Description of the Structure of Molecular and Layered Crystals: Ab

https://doi.org/10.1021/acselectrochem.6c00077
ACS Electrochem. XXXX, XXX, XXX−XXX

Initio DFT Calculations with van der Waals Corrections. *J. Phys. Chem. A* **2010**, *114* (43), 11814−11824.
(58) Nørskov, J. K.; Rossmeisl, J.; Logadottir, A.; Lindqvist, L.; Kitchin, J. R.; Bligaard, T.; Jónsson, H. Origin of the Overpotential for Oxygen Reduction at a Fuel-Cell Cathode. *J. Phys. Chem. B* **2004**, *108* (46), 17886−17892.
(59) Birdja, Y. Y.; Pérez-Gallent, E.; Figueiredo, M. C.; Göttle, A. J.; Calle-Vallejo, F.; Koper, M. T. M. Advances and challenges in understanding the electrocatalytic conversion of carbon dioxide to fuels. *Nat. Energy* **2019**, *4* (9), 732−745.
(60) Vavra, J.; Ramona, G. P. L.; Dattila, F.; Kormányos, A.; Priamushko, T.; Albertini, P. P.; Loiudice, A.; Cherevko, S.; Lopéz, N.; Buonsanti, R. Solution-based Cu+ transient species mediate the reconstruction of copper electrocatalysts for CO_2 reduction. *Nat. Catal.* **2024**, *7* (1), 89−97.
(61) Amirbeigiarab, R.; Tian, J.; Herzog, A.; Qiu, C.; Bergmann, A.; Roldan Cuenya, B.; Magnussen, O. M. Atomic-scale surface restructuring of copper electrodes under CO_2 electroreduction conditions. *Nat. Catal.* **2023**, *6* (9), 837−846.
(62) Laboratories, B.-R. *Chelex 100 and Chelex 20 Chelating Ion Exchange Resin: Instruction Manual*.
(63) Fuller, L.; Zhang, G.; Noh, S.; Van Lehn, R. C.; Schreier, M. Electrolyte Anions Suppress Hydrogen Generation in Electrochemical CO Reduction on Cu. *Angew. Chem., Int. Ed.* **2025**, *64* (10), No. e202421196.
(64) Dutta, N.; Bagchi, D.; Chawla, G.; Peter, S. C. A Guideline to Determine Faradaic Efficiency in Electrochemical CO_2 Reduction. *ACS Energy Lett.* **2024**, *9* (1), 323−328.
(65) Kresse, G.; Furthmüller, J. Efficiency of ab-initio total energy calculations for metals and semiconductors using a plane-wave basis set. *Comput. Mater. Sci.* **1996**, *6* (1), 15−50.
(66) Kresse, G.; Furthmüller, J. Efficient iterative schemes for ab initio total-energy calculations using a plane-wave basis set. *Phys. Rev. B* **1996**, *54* (16), 11169−11186.
(67) Almora-Barrios, N.; Carchini, G.; Blonski, P.; Lopez, N. Costless Derivation of Dispersion Coefficients for Metal Surfaces. *J. Chem. Theory Comput.* **2014**, *10* (11), 5002−5009.
(68) Blöchl, P. E. Projector augmented-wave method. *Phys. Rev. B* **1994**, *50* (24), 17953−17979.
(69) Kresse, G.; Joubert, D. From ultrasoft pseudopotentials to the projector augmented-wave method. *Phys. Rev. B* **1999**, *59* (3), 1758−1775.
(70) Hjorth Larsen, A.; Jorgen Mortensen, J.; Blomqvist, J.; Castelli, I. E.; Christensen, R.; Dulak, M.; Friis, J.; Groves, M. N.; Hammer, B.; Hargus, C.; et al. The atomic simulation environment-a Python library for working with atoms. *J. Phys. Condens. Matter.* **2017**, *29* (27), No. 273002.
(71) Pack, J. D.; Monkhorst, H. J. "Special points for Brillouin-zone integrations"—a reply. *Phys. Rev. B* **1977**, *16* (4), 1748−1749.
(72) Makov, G.; Payne, M. C. Periodic boundary conditions in ab initio calculations. *Phys. Rev. B* **1995**, *51* (7), 4014−4022.
(73) Alvarez-Moreno, M.; de Graaf, C.; Lopez, N.; Maseras, F.; Poblet, J. M.; Bo, C. Managing the computational chemistry big data problem: the ioChem-BD platform. *J. Chem. Inf. Model.* **2015**, *55* (1), 95−103.

https://doi.org/10.1021/acselectrochem.6c00077
ACS Electrochem. XXXX, XXX, XXX−XXX